

A second-order unconditionally stable method for the anisotropic dendritic crystal growth model with an orientation-field

Yibao Li^a, Kang Qin^a, Qing Xia^a, Junseok Kim^{b,*}

^a School of Mathematics and Statistics, Xi'an Jiaotong University, Xi'an 710049, China

^b Department of Mathematics, Korea University, Seoul 02841, Republic of Korea

ARTICLE INFO

Article history:

Received 15 April 2022

Received in revised form 2 August 2022

Accepted 7 November 2022

Available online 11 November 2022

Keywords:

Phase field model

Crystal growth model

Anisotropy

Unconditionally energy-stable

Orientalional field model

ABSTRACT

In this article, we develop a linear, unconditionally energy stable computational scheme for solving the dendritic crystal growth model with the orientational field. We apply the phase field model to describe the evolution of crystal with rotation. The model, which couples the heat equation and anisotropic Allen–Cahn type equation, is a complicated nonlinear system. The time integration is based on the second-order Crank–Nicolson method. The anisotropic coefficient is treated by using the invariant energy quadratization. We mathematically prove that the proposed method is unconditionally energy stable. The second-order spatial and temporal accuracy will be preserved for the numerical approximation. Various computational tests are performed to show the accuracy, stability, and efficiency of the proposed scheme.

© 2022 IMACS. Published by Elsevier B.V. All rights reserved.

1. Introduction

The micro-structure of grain controls many material properties [1,3,14], whose internal boundaries play important roles in the study of materials behavior [4,35]. The development of micro-structure is influenced by the orientation selection of the crystal tip [17,18], whose position and velocity are the significant parameters in the phase-field simulation. The naturally growing dendrites possess a unique steady crystal tip, characterized by its velocity, radius of curvature, and shape, which leads to a time-dependent side branched dendrite as it propagates [9]. Understanding the complexity of crystallization is vitally important for several physical processes, such as phase transition on molten pool in additive manufacturing process [19,47], investigation of the physical properties for materials [8], and micro-structural design during protein crystallization [30]. The phase-field method has been intensively employed as a tool to model the evolution of crystallization [39,49], which has shown strong robustness in many other applications, such as coupling calculation of multiple physical fields on manifold [36,37], topology optimization [20,46], and image processing [21]. P. Stefanovic et al. [25] introduced a modified phase field crystal method to investigate many phase transformation phenomena in material processing. I. Singer-Loginova and L. Gránásky [7,24] reviewed the advances in the orientation field based phase field model which incorporates homogeneous and heterogeneous nucleation of growth centers and mechanisms to generate new grains at the boundary of crystals. S. Tang et al. [28,29] investigated the orientation selection of the cubic dendrite growth at the atomic scale by considering the

* Corresponding author.

E-mail addresses: yibaoli@xjtu.edu.cn (Y. Li), cfdkim@korea.ac.kr (J. Kim).

URLs: <http://gr.xjtu.edu.cn/web/yibaoli> (Y. Li), <https://mathematicians.korea.ac.kr/cfdkim> (J. Kim).

relationship among growth morphology, velocity, and density distribution. K. R. Elder et al. [2] examined the relationship between the classical density functional theory of freezing and phase-field modeling. Microstructure of industrial materials is affected by the orientation selection of the crystal [34,45]. R. Kobayashi et al. [12] developed a two-dimensional frame-invariant phase field model of grain boundaries, whose dynamic solutions are presented showing rotation of a small grain between two pinned grains. Korbuly et al. [13] compared two phase-field theories for polycrystalline solidification with orientation fields. The authors studied the grain coarsening process including the limiting grain size distribution. Li et al. [15] developed a phase-field model with orientational field for polycrystalline solidification in binary alloys. By involving the arbitrary crystallographic orientation, realistic solidification microstructures can be produced. However, there are very few published attempts in designing efficient and energy stable methods for the highly nonlinear system by considering the time-dependent orientation field due to the complexity of the coupling relationship in the anisotropic dendritic model.

Up to now, there are some successful attempts in developing efficient and energy stable numerical methods for crystal growth without considering the influence of orientation. For the highly nonlinear crystal growth models, several efficient algorithms have been applied with good results, such as adaptive mesh method [18], Scalar Auxiliary Variable method [38], non-linear multigrid method [10], and Invariant Energy Quadraticization (IEQ) method [48]. Considering the highly non-linear coupling relationship, we aimed to use the IEQ method to establish a decoupled, linear, energy stable method by enforcing the free-energy density as an invariant, quadratic functional under the influence of orientation [51]. X. Yang applied various mathematically deep publications [40–44] in the development of numerical approximation. They coupled the anisotropic Allen–Cahn (AC) type equation with the heat equation to establish the highly nonlinear system for phase field dendritic crystal growth. These extensive works are based on the IEQ approach, which can remove the numerical oscillations and enhance the stability, to obtain the unconditionally energy stable and decoupled system with the required accuracy. J. Zhao et al. [50,51] considered a phase field dendritic crystal growth equation with a temperature-dependent potential and a gradient-dependent anisotropic coefficient. Motivated by the novel IEQ method, Y. Gong et al. [5,6,23] aimed to develop the high-order semi-discretized scheme. Under the IEQ framework, they presented linear methods based on prediction-correction schemes. J. Zhang et al. [49] combined the stabilized IEQ scheme with a decoupling method which requires solving only linear elliptic equations. They rigorously proved the unconditional energy stability and presented many computational experiments to show the stability and accuracy. However, there are few studies that have investigated the coupling relationship between the anisotropic crystallization and orientation because of the complexity of the nonlinear terms. Warren et al. [32] considered an anisotropic phase-field dendritic crystal growth model with orientation and proposed a finite difference scheme to capture the grain boundaries with the spatially second-order and temporally first-order accuracies. Inspired by [32,33], we consider the coupling relationship between the orientation and phase fields. We aim to establish an efficient, decoupled and linear system to investigate the influence of orientation on the crystallization.

In this study, we propose a highly non-linear system consists of three coupled equations: the heat transfer equation, the AC equation with a gradient-dependent anisotropic coefficient, and the heat equation. Compared to the isotropic phase field model, there are some challenges for solving the system, for example, how to deal with the anisotropic coefficient and the nonlinearly coupled heat transfer term. We want to develop a numerical scheme which is temporally high-order accurate, unconditionally energy stable, and simple to implement. For this purpose, we develop a linear, temporally and spatially second-order accurate numerical method. The proposed system has been rigorously proved to be unconditionally stable, which implies that a large time step can be used. The governing equations are solved by the multigrid method. Various computational tests are performed to show the accuracy, stability, and efficiency of the proposed method.

The outline of this paper is the following. In Section 2, we describe the governing system. In Section 3, we discretize the system and develop a temporally second-order accurate and unconditionally energy stable method. In Section 4, we show the numerical results using the proposed method. Finally, some conclusions are drawn in Section 5.

2. Governing equations and energy dissipation law

We briefly describe the anisotropic phase field model for dendritic crystal growth [11,12,15,33]. A scalar order parameter $\phi(x, t)$ describes the liquid ($\phi = -1$) and solid ($\phi = 1$) phases. The total free energy functional is given as

$$E = \int_{\Omega} \left(\frac{\varepsilon_{\phi}^2}{2} |\kappa(\nabla\phi - \theta)\nabla\phi|^2 + sg(\phi)|\nabla\theta| + F(\phi) + \frac{\varepsilon_{\phi}\lambda}{2K} |T - T_m|^2 \right) d\mathbf{x}, \quad (1)$$

where ε_{ϕ} , λ , s and K are positive parameters. Here, we use $T(x, t)$ and $\theta(x, t)$ to denote the temperature and orientation fields, respectively. For the two-dimensional (2D) system, the anisotropy coefficient $\kappa(\nabla\phi - \theta)$ is given by

$$\kappa(\nabla\phi - \theta) = 1 + \varepsilon_4 \cos(m(\vartheta - \theta)), \quad (2)$$

where m and ε_4 are the number of folds of anisotropy and anisotropy strength parameter, respectively. The inclination of the normal to the liquid–solid interface with respect to the x -axis is $\tan \vartheta$, where $\vartheta = \arctan(\phi_y/\phi_x)$ is the orientation of the interface. Then, we can rotate into the crystal frame by using the angle $\vartheta - \theta$ when calculating the effects of anisotropy [33]. It is easy to see $\kappa(\nabla\phi + 2\pi/m) = \kappa(\nabla\phi)$ for a crystal possessing m fold rotation symmetry. For example, when $m = 4$, $\kappa(\nabla\phi - \theta)$ can be rewritten as

$$\kappa(\nabla\phi - \theta) = 1 + \varepsilon_4 \left(\cos(4 \arctan \nabla\phi) \cos(4\theta) + \sin(4 \arctan \nabla\phi) \sin(4\theta) \right), \quad (3)$$

where $\cos(4 \arctan \nabla\phi) = 4(\phi_x^4 + \phi_y^4)/|\nabla\phi|^4 - 3$ and $\sin(4 \arctan \nabla\phi) = 4\phi_x\phi_y(\phi_x^2 - \phi_y^2)/|\nabla\phi|^4$. The parameter s specifies the strength of the coupling between ϕ and $\nabla\theta$ while $g(\phi) = (\phi + 1)^2$ is used to reduce or eliminate the effects of crystalline orientation [33]. The orientational contribution $sg(\phi)|\nabla\theta|$ represents the excess free energy due to inhomogeneities in crystal orientation in space [15]. We use $F(\phi) = (\phi^2 - 1)^2/4$ to be the double well potential. For the last term of Eq. (1), we refer to [11,41] and take it as the conformational entropy, where T_m is the melting point of the crystal. We should note that there are different expressions of enthalpy energy for convective latent heat effects considering the thermodynamical consistent systems [16,26] where the hydrodynamic effects and thermal-hydrodynamic coupling were incorporated. The internal energy has been considered as a function of the absolute temperature and phase variable. Their thermodynamically consistent model for dendritic crystal growth is derived from the first and second law of thermodynamics and has been rigorously proved to be energy and entropy production preserved. Using the L^2 -gradient flow for the energy functional, we obtain the following equations:

$$\tau_\phi \phi_t = -\frac{\delta E}{\delta \phi} - p(\phi)\lambda\varepsilon_\phi(T - T_m) = \varepsilon_\phi^2 \nabla \cdot (\kappa^2(\nabla\phi - \theta)\nabla\phi + \kappa(\nabla\phi - \theta)|\nabla\phi|^2 \mathbf{H}_\phi) \quad (4a)$$

$$- F'(\phi) - sg'(\phi)|\nabla\theta| - p(\phi)\lambda\varepsilon_\phi(T - T_m),$$

$$\theta_t = -\frac{\delta E}{\delta \theta} = \nabla \cdot (sg(\phi)\frac{\nabla\theta}{|\nabla\theta|}) - \varepsilon_\phi^2 |\nabla\phi|^2 \kappa(\nabla\phi - \theta) \mathbf{H}_\theta, \quad (4b)$$

$$T_t = D\Delta T + Kp(\phi)\phi_t, \quad (4c)$$

where \mathbf{H}_ϕ and \mathbf{H}_θ are the variational derivatives of $\kappa(\nabla\phi - \theta)$ with respect to ϕ and θ , respectively. In two-dimensional space, we choose

$$\mathbf{H}_\phi = \frac{\delta \kappa(\nabla\phi - \theta)}{\delta \phi} = \frac{16\varepsilon_4}{|\nabla\phi|^6} \left(\phi_x(\phi_x^2\phi_y^2 - \phi_y^4) \cos 4\theta + \phi_y(\phi_y^4 + \phi_x^4 - 6\phi_y^2\phi_x^2) \sin 4\theta, \right. \\ \left. (\phi_y(\phi_x^2\phi_y^2 - \phi_x^4)) \cos 4\theta - \phi_x(\phi_x^4 + \phi_y^4 - 6\phi_x^2\phi_y^2) \sin 4\theta \right), \quad (5a)$$

$$\mathbf{H}_\theta = \frac{\delta \kappa(\nabla\phi - \theta)}{\delta \theta} = 16\varepsilon_4 \left(\frac{\phi_x\phi_y(\phi_x^2 - \phi_y^2)}{|\nabla\phi|^4} \cos(4\theta) - \left(\frac{\phi_x^4 + \phi_y^4}{|\nabla\phi|^4} - \frac{3}{4} \right) \sin(4\theta) \right). \quad (5b)$$

Here, $\tau(\phi)$ is the positive mobility [32] and D is the diffusion coefficient. The function $p(\phi)$ is the generation of latent heat and can be defined as $p(\phi) = \phi^4 - 2\phi^2 + 1$ [32] or $p(\phi) = 1 - \phi^2$ [31]. We use the periodic or zero Neumann boundary condition. Equations (Eqs. (4a)–(4c)) satisfy the energy dissipation law. We denote the continuous versions of L^2 inner product of any two functions $f_1(x)$ and $f_2(x)$ by $(f_1(x), f_2(x)) = \int_\Omega f_1(x)f_2(x)dx$. The L^2 norm of the function $f(x)$ by $\|f\|^2 = (f, f)$. By taking the L^2 inner product of Eq. (4a) with ϕ_t , of Eq. (4b) with θ_t , and of Eq. (4c) with $\lambda\varepsilon_\phi(T - T_m)/K$, we obtain

$$(\tau_\phi \phi_t, \phi_t) = \left(-\frac{\delta E}{\delta \phi} - p(\phi)\lambda\varepsilon_\phi(T - T_m), \phi_t \right), \quad (6a)$$

$$(\theta_t, \theta_t) = \left(-\frac{\delta E}{\delta \theta}, \theta_t \right), \quad (6b)$$

$$(T_t, \frac{\lambda\varepsilon_\phi}{K}(T - T_m)) = (D\Delta T + Kp(\phi)\phi_t, \frac{\lambda\varepsilon_\phi}{K}(T - T_m)). \quad (6c)$$

Therefore, by substituting Eq. (6) into the energy equation, the system can be rewritten as

$$\begin{aligned} \frac{d}{dt} E(\phi, \theta, T) &= \frac{\delta E}{\delta \phi} \phi_t + \frac{\delta E}{\delta \theta} \theta_t + \frac{\delta E}{\delta T} T_t \\ &= -(\tau_\phi \phi_t, \phi_t) - p(\phi)\lambda\varepsilon_\phi(T - T_m, \phi_t) - (\theta_t, \theta_t) + \frac{D\lambda\varepsilon}{K} (\Delta T, T - T_m) \\ &\quad + p(\phi)\lambda\varepsilon_\phi(T - T_m, \phi_t) \\ &= -(\|\sqrt{\tau_\phi} \phi_t\|^2 + \|\theta_t\|^2 + \frac{D\lambda\varepsilon}{K} \|\nabla(T - T_m)\|^2) \leq 0. \end{aligned} \quad (7)$$

Let us define the auxiliary variable as follows:

$$U = \sqrt{\frac{\varepsilon_\phi^2}{2} |\kappa(\nabla\phi - \theta)\nabla\phi|^2 + sg(\phi)|\nabla\theta| + F(\phi) + B}, \quad (8)$$

where B is a constant. Thus, the total free energy (Eq. (1)) can be rewritten as:

$$E = \int_{\Omega} U^2 + \frac{\lambda \varepsilon_{\phi}}{2K} |T - T_m|^2 - B d\mathbf{x}. \quad (9)$$

By taking the time derivative of the new variable U , we rewrite the system Eqs. (4a)–(4c) as the following equivalent system,

$$\tau_{\phi} \phi_t = -Z_{\phi} U - \lambda \varepsilon_{\phi} p(T - T_m), \quad (10a)$$

$$\theta_t = -Z_{\theta} U, \quad (10b)$$

$$U_t = \frac{1}{2} Z_{\phi} \phi_t + \frac{1}{2} Z_{\theta} \theta_t, \quad (10c)$$

$$T_t = D \Delta T + K p' \phi_t, \quad (10d)$$

where

$$Z_{\phi} = \frac{-\varepsilon_{\phi}^2 \nabla \cdot (\kappa (\nabla \phi - \theta)^2 \nabla \phi + \kappa (\nabla \phi - \theta) |\nabla \phi|^2 \mathbf{H}_{\phi}) + s g'(\phi) |\nabla \theta| + f(\phi)}{\sqrt{\frac{\varepsilon_{\phi}^2}{2} |\kappa (\nabla \phi - \theta) \nabla \phi|^2 + s g(\phi) |\nabla \theta| + F(\phi) + B}}, \quad (11a)$$

$$Z_{\theta} = \frac{-\nabla \cdot (s g(\phi) \frac{\nabla \theta}{|\nabla \theta|}) + \varepsilon_{\phi}^2 |\nabla \phi|^2 \kappa (\nabla \phi - \theta) \mathbf{H}_{\theta}}{\sqrt{\frac{\varepsilon_{\phi}^2}{2} |\kappa (\nabla \phi - \theta) \nabla \phi|^2 + s g(\phi) |\nabla \theta| + F(\phi) + B}}. \quad (11b)$$

The system (Eqs. (10a)–(10d)) satisfies an energy dissipative law in terms of ϕ , T , θ and U . By taking the L^2 inner product of Eq. (10a) with ϕ_t , of Eq. (10b) with θ_t , of Eq. (10c) with $2U$, of Eq. (10d) with $\lambda \varepsilon_{\phi} (T - T_m)/K$, we have the energy dissipation law of the new system Eqs. (10a)–(10d) as:

$$\frac{d}{dt} E(\phi, \theta, U, T) = -\tau_{\phi} \|\phi_t\|^2 - \frac{D \lambda \varepsilon_{\phi}}{K} \|\nabla (T - T_m)\|^2 - \|\theta_t\|^2 \leq 0. \quad (12)$$

3. Numerical schemes

We consider an unconditionally energy-stable and temporally second-order accurate method for Eqs. (4a)–(4c). The numerical domain is $\Omega = [0, L] \times [0, L]$. The spatial step size is $h = L/N_x = L/N_y$, where N_x and N_y are even integers. The time step is $\delta t = T_{time}/N_t$, where T_{time} is the final time and N_t is the number of total time steps. We denote $\phi_{i,j}^n = \phi(x_i, y_j, n\delta t)$, where $(x_i, y_j) = (ih, jh)$ for $i = 0, \dots, N_x$, $j = 0, \dots, N_y$. The proposed numerical methods should follow the new energy dissipation law Eq. (12) in the discrete sense. We develop a temporally second-order method for solving the system Eqs. (10a)–(10d) based on the second-order Crank–Nicolson (CN) scheme:

$$\tau_{\phi} \frac{\phi^{n+1} - \phi^n}{\delta t} = -\hat{Z}_{\phi}^{n+1/2} U^{n+1} - \lambda \varepsilon_{\phi} p(\hat{\phi}^{n+1/2})(T^{n+1/2} - T_m) \quad (13a)$$

$$\frac{\theta^{n+1} - \theta^n}{\delta t} = -\hat{Z}_{\theta}^{n+1/2} U^{n+1} \quad (13b)$$

$$\frac{U^{n+1} - U^n}{\delta t} = \frac{1}{2} \hat{Z}_{\phi}^{n+1/2} \frac{\phi^{n+1} - \phi^n}{\delta t} + \frac{1}{2} \hat{Z}_{\theta}^{n+1/2} \frac{\theta^{n+1} - \theta^n}{\delta t} \quad (13c)$$

$$\frac{T^{n+1} - T^n}{\delta t} = D \Delta_d T^{n+1/2} + K p(\hat{\phi}^{n+1/2}) \frac{\phi^{n+1} - \phi^n}{\delta t}, \quad (13d)$$

where $\hat{\phi}^{n+1/2} = \frac{3}{2} \phi^n - \frac{1}{2} \phi^{n-1}$, $\hat{\theta}^{n+1} = \frac{3}{2} \theta^n - \frac{1}{2} \theta^{n-1}$, $\hat{Z}_{\theta}^{n+1/2} = \frac{3}{2} Z_{\theta}^n - \frac{1}{2} Z_{\theta}^{n-1}$, $\hat{Z}_{\phi}^{n+1/2} = \frac{3}{2} Z_{\phi}^n - \frac{1}{2} Z_{\phi}^{n-1}$. We use Δ_d to denote the discrete Laplace operator i.e., $\Delta_d(\cdot)_{i,j} = ((\cdot)_{i+1,j} + (\cdot)_{i-1,j} + (\cdot)_{i,j+1} + (\cdot)_{i,j-1} - 4(\cdot)_{i,j})/h^2$. We should note that U will not add heavy computations because we can rewrite Eq. (13c) as follows

$$U^{n+1} = \frac{1}{2} \hat{Z}_{\phi}^{n+1/2} \phi^{n+1} + \frac{1}{2} \hat{Z}_{\theta}^{n+1/2} \theta^{n+1} + A, \quad (14)$$

where $A = U^n - \frac{1}{2} \hat{Z}_{\phi}^{n+1/2} \phi^n - \frac{1}{2} \hat{Z}_{\theta}^{n+1/2} \theta^n$. By substituting Eq. (14) to Eq. (13a) and Eq. (13b), the system Eqs. (13a)–(13d) can be rewritten as follows

$$\Gamma_1(\phi^{n+1}) + \frac{1}{2} \hat{Z}_\phi^{n+1/2} \hat{Z}_\theta^{n+1/2} \theta^{n+1} + \lambda \varepsilon_\phi \hat{p}(\phi^{n+1/2}) T^{n+1} = f_1, \quad (15a)$$

$$\Gamma_2(\theta^{n+1}) + \frac{1}{2} \hat{Z}_\phi^{n+1/2} \hat{Z}_\theta^{n+1/2} \phi^{n+1} = f_2, \quad (15b)$$

$$T^{n+1} - \frac{D}{\delta t} \Delta T^{n+1} - \hat{p}(\phi^{n+1/2}) \phi^{n+1} = f_3, \quad (15c)$$

where $\Gamma_1(\phi^{n+1}) = \frac{\tau_\phi}{\delta t} \phi^{n+1} + \frac{1}{2} (\hat{Z}_\phi^{n+1/2})^2 \phi^{n+1}$, $\Gamma_2(\theta^{n+1}) = \frac{1}{\delta t} \theta^{n+1} + \frac{1}{2} (\hat{Z}_\theta^{n+1/2})^2 \theta^{n+1}$ and $f_1 = \Gamma_1(\phi^n) + \frac{1}{2} \hat{Z}_\phi^{n+1/2} \hat{Z}_\theta^{n+1/2} \theta^n$, $f_2 = \Gamma_2(\theta^n) + \frac{1}{2} \hat{Z}_\phi^{n+1/2} \hat{Z}_\theta^{n+1/2} \phi^n$, $f_3 = T^n - \hat{p}'(\phi^{n+1/2}) \phi^n$. We solve Eqs. (15a)–(15c) directly to obtain ϕ^{n+1} , T^{n+1} and θ^{n+1} , and then update the variable U^{n+1} from Eq. (14). We denote the discrete L^2 inner product of any two discrete functions $f_1(x)$ and $f_2(x)$ by $(f_1(x), f_2(x))_d = \sum_{j=1}^{N_y} \sum_{i=1}^{N_x} f_1(x_{i,j}) f_2(x_{i,j})$. The L^2 norm of the discrete function $f(x)$ by $\|f\|_d^2 = (f, f)_d$.

Theorem 1. The scheme, Eqs. (13a)–(13d), is unconditionally energy stable and satisfies the following discrete energy dissipation law.

$$\begin{aligned} E_d^{n+1} - E_d^n &= -\frac{\delta t D \lambda \varepsilon_\phi}{2K} \|\nabla_d(T^{n+1} - T_m)\|_d^2 - \frac{\delta t D \lambda \varepsilon_\phi}{2K} \|\nabla_d(T^n - T_m)\|_d^2 \\ &\quad - \left(\|U^{n+1} - U^n\|_d^2 + \tau_\phi \frac{\|\phi^{n+1} - \phi^n\|_d^2}{\delta t} + \frac{1}{\delta t} \|\theta^{n+1} - \theta^n\|_d^2 \right) \leq 0, \end{aligned} \quad (16)$$

where $E_d^n(\phi^n, \theta^n, U^n, T^n) = U^n + \lambda \varepsilon_\phi \|T^n - T_m\|_d^2/k - B$.

Proof. By taking the L^2 inner product of Eq. (13a) with $\phi^{n+1} - \phi^n$, we get

$$\begin{aligned} &\left(\tau_\phi \frac{\phi^{n+1} - \phi^n}{\delta t}, \phi^{n+1} - \phi^n \right)_d \\ &= \left(-\hat{Z}_\phi^{n+1/2} U^{n+1}, \phi^{n+1} - \phi^n \right)_d + \left(-\lambda \varepsilon_\phi \hat{p}(\hat{\phi}^{n+1/2}) (T^{n+1/2} - T_m), \phi^{n+1} - \phi^n \right)_d. \end{aligned} \quad (17)$$

By taking the L^2 inner product of Eq. (13b) with $\theta^{n+1} - \theta^n$, we obtain

$$\left(\frac{\theta^{n+1} - \theta^n}{\delta t}, \theta^{n+1} - \theta^n \right)_d = \left(-\hat{Z}_\theta^{n+1/2} U^{n+1}, \theta^{n+1} - \theta^n \right)_d. \quad (18)$$

By taking the L^2 inner product of Eq. (13c) with $2U^{n+1}$, we obtain

$$\left(\frac{U^{n+1} - U^n}{\delta t}, 2U^{n+1} \right)_d = \left(\frac{1}{2} \hat{Z}_\phi^{n+1/2} \frac{\phi^{n+1} - \phi^n}{\delta t} + \frac{1}{2} \hat{Z}_\theta^{n+1/2} \frac{\theta^{n+1} - \theta^n}{\delta t}, 2U^{n+1} \right)_d, \quad (19a)$$

$$\|U^{n+1}\|_d^2 - \|U^n\|_d^2 + \|U^{n+1} - U^n\|_d^2 = \left(\hat{Z}_\phi^{n+1/2} (\phi^{n+1} - \phi^n) + \hat{Z}_\theta^{n+1/2} (\theta^{n+1} - \theta^n), U^{n+1} \right)_d. \quad (19b)$$

By taking the L^2 inner product of Eq. (13d) with $\lambda \varepsilon_\phi K (T^{n+1/2} - T_m)/K$ and performing integration by parts, we get

$$\begin{aligned} &\left(T^{n+1} - T^n, \frac{\lambda \varepsilon_\phi}{K} (T^{n+1/2} - T_m) \right)_d \\ &= \left(\delta t D \Delta_d T^{n+1/2}, \frac{\lambda \varepsilon_\phi}{K} (T^{n+1/2} - T_m) \right)_d + \left(K p(\hat{\phi}^{n+1/2}) (\phi^{n+1} - \phi^n), \frac{\lambda \varepsilon_\phi}{K} (T^{n+1/2} - T_m) \right)_d \\ &= \frac{\delta t D \lambda \varepsilon_\phi}{2K} \left(\Delta_d (T^{n+1} + T^n), (T^{n+1} - T_m) + (T^n - T_m) \right)_d \\ &\quad + \left(K p(\hat{\phi}^{n+1/2}) (\phi^{n+1} - \phi^n), \frac{\lambda \varepsilon_\phi}{K} (T^{n+1/2} - T_m) \right)_d \\ &= -\frac{\delta t D \lambda \varepsilon_\phi}{2K} \|\nabla_d(T^{n+1} - T_m)\|_d^2 - \frac{\delta t D \lambda \varepsilon_\phi}{2K} \|\nabla_d(T^n - T_m)\|_d^2 \\ &\quad + \left(K p(\hat{\phi}^{n+1/2}) (\phi^{n+1} - \phi^n), \frac{\lambda \varepsilon_\phi}{K} (T^{n+1/2} - T_m) \right)_d. \end{aligned} \quad (20)$$

The left equation can be rewritten as

$$\begin{aligned} &\left(T^{n+1} - T^n, \frac{\lambda \varepsilon_\phi}{K} (T^{n+1/2} - T_m) \right)_d \\ &= \frac{\lambda \varepsilon_\phi}{2K} \left((T^{n+1} - T_m) - (T^n - T_m), (T^{n+1} - T_m) + (T^n - T_m) \right)_d \\ &= \frac{\lambda \varepsilon_\phi}{2K} \left(\|T^{n+1} - T_m\|_d^2 - \|T^n - T_m\|_d^2 \right). \end{aligned} \quad (21)$$

Table 1Error and convergence result with various mesh grids, the temporal size is $\Delta t = 10^{-9}$.

Grid size	64 × 64	128 × 128	256 × 256
l_2 -error of ϕ	3.8201e-2	1.0150e-2	2.7541e-3
Rate	1.906	1.891	
l_2 -error of T	4.0401e-2	1.0082e-2	2.7291e-3
Rate	2.010	1.972	

Then, substitute Eqs. (21) into Eq. (20), we can obtain

$$\begin{aligned} & \frac{\lambda \varepsilon \phi}{2K} \left(\|T^{n+1} - T_m\|_d^2 - \|T^n - T_m\|_d^2 \right) \\ &= -\frac{\delta t D \lambda \varepsilon \phi}{2K} \|\nabla_d(T^{n+1} - T_m)\|_d^2 - \frac{\delta t D \lambda \varepsilon \phi}{2K} (\|\nabla_d T^n - T_m\|_d^2) \\ & \quad + \left(Kp(\hat{\phi}^{n+1/2})(\phi^{n+1} - \phi^n), \frac{\lambda \varepsilon \phi}{K}(T^{n+1/2} - T_m) \right)_d. \end{aligned} \quad (22)$$

Finally, by summing Eqs. (17), (18), (19b), and (22) up, we get

$$\begin{aligned} & E_d^{n+1} - E_d^n \\ &= \|U^{n+1}\|_d^2 - \|U^n\|_d^2 + \frac{\lambda \varepsilon \phi}{2K} \left(\|T^{n+1} - T_m\|_d^2 - \|T^n - T_m\|_d^2 \right) \\ &= -\frac{\delta t D \lambda \varepsilon \phi}{2K} \|\nabla_d(T^{n+1} - T_m)\|_d^2 - \frac{\delta t D \lambda \varepsilon \phi}{2K} \|\nabla_d(T^n - T_m)\|_d^2 \\ & \quad - \left(\|U^{n+1} - U^n\|_d^2 + \tau_\phi \|\phi^{n+1} - \phi^n\|_d^2 / \delta t + \|\theta^{n+1} - \theta^n\|_d^2 / \delta t \right) \leq 0. \end{aligned} \quad (23)$$

The proof is completed. \square

Remark 1. The Allen–Cahn equation with a gradient-dependent anisotropic coefficient is derived from the L^2 space by the variational gradient flow method. Refer to the stability analysis in [10,27], we can prove the unconditional stability based on the full discretization. Furthermore, the system admits a unique solution ϕ in L^2 , while the H^1 bound of the numerical solution cannot be justified theoretically. This brings up some issues for guaranteeing the stability. For the well-posedness of the weak form of the proposed system, we suggest to refer the references [10,22,41].

4. Numerical simulations

Now, we present various computational experiments to demonstrate the accuracy, energy stability, and efficiency. Unless otherwise specified, the computational domain is $[0, 2\pi] \times [0, 2\pi]$ with a 512×512 mesh grid. The parameters are chosen as $\tau_\phi = 0.5519$, $\varepsilon_\phi = 1.12e - 2$, $\varepsilon_4 = 0.05$, $D = 2.25e - 4$, $K = 0.5$, $B = 5$, $T_m = 0$ and $\lambda = 380$.

4.1. Convergence test

We perform two computational tests to confirm that the second-order spatial and temporal convergence of the proposed method. We use a manufactured solution technique. We use the exact solutions as follows:

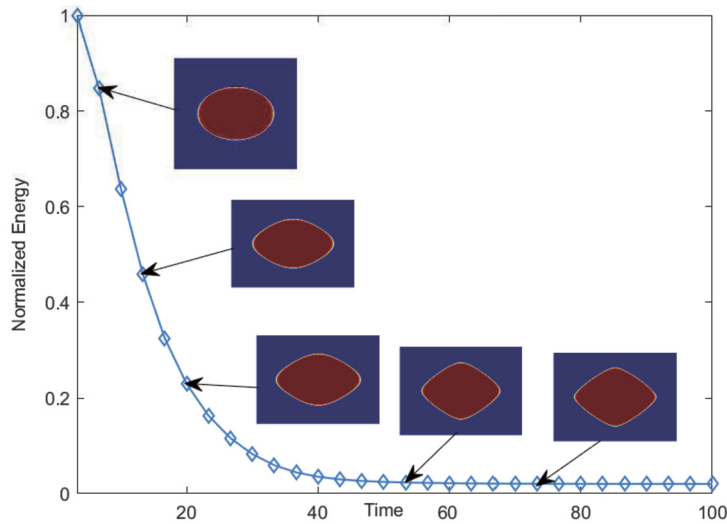
$$\phi(x, y, t) = \cos(2x) \cos(4y) \cos(t), \quad T(x, y, t) = \cos(4x) \cos(2y) \cos(t), \quad \theta(x, y, t) = 0. \quad (24)$$

We define the error e_ϕ^h and e_T^h as $e_{ij}^{\phi(h)} = \phi_{ij}^{ref} - \phi_{ij}^h$ and $e_{ij}^{T(h)} = T_{ij}^{ref} - T_{ij}^h$. The convergence rate is defined as $\log_2(\|e_h\|_2 / \|e_{h/2}\|_2)$, where $\|e\|_2^2$ is the discrete l_2 norm defined as $\|e\|_2^2 = \sum_{i=1}^{N_x} \sum_{j=1}^{N_y} (N_x N_y)$. Table 1 lists the errors and rates of convergence, which shows the second-order accuracy with respect to the space.

Next, we fix the mesh size as 256×256 and choose a set of time-steps $\delta t = 0.02$, 0.01 , and 0.005 . Numerical solutions are calculated up to time $T_{time} = 1$. We define the error of a grid to be $e_{ij}^{\phi(\delta t)} = \phi_{ij}^{ref} - \phi_{ij}^{\delta t}$ and $e_{ij}^{T(\delta t)} = T_{ij}^{ref} - T_{ij}^{\delta t}$. In Table 2, the mesh size is 256×256 and the time step sizes δt are 0.02 , 0.01 , and 0.005 . The results of Table 1 and 2 imply that our proposed method are second-order accurate in both time and space.

Table 2Error and convergence result with various temporal sizes, the mesh grid is 256×256 .

Temporal step	0.02		0.01		0.005
l_2 -error of ϕ	2.6451e-2		7.3530e-3		1.7032e-3
Rate		1.847		2.142	
l_2 -error of T	2.9561e-2		7.1404e-3		1.7502e-3
Rate		2.059		2.029	

**Fig. 1.** Temporal evolutions of the total free energy functional using the IEQ method, with time steps $\delta t = 0.01$.

4.2. Decreasing discrete energy

To validate the unconditional energy dissipation, we consider the time step $\delta t = 0.01$. We set the initial condition as

$$\phi(x, y, t) = \tanh\left(\frac{1.5 - \sqrt{(x - \pi)^2 + (y - \pi)^2}}{\epsilon}\right), \quad T(x, y, t) = 0, \quad \theta(x, y, t) = 0. \quad (25)$$

Here we consider the model parameters as $\tau_\phi = 1000$, $\lambda = 200$, $D = 1e-4$, $\varepsilon_\phi = 0.02$, $T_m = 0$, $K = 10$, $\varepsilon_4 = 0$, $B = 5$. We normalize the total energy by the initial energy. The subfigures in Fig. 1 are the evolution of crystallization. It is obvious that the initial circular shape gradually evolves into a rhombus. Furthermore, we can observe that the energy evolution curve is monotonically decaying, which verifies that the proposed scheme is stable.

Because the proposed system contains the strong nonlinear term, it is significant to avoid the time-step restrictions for stability. To show the stability of the proposed method, we plot the evolution curves of the total free energy in Fig. 2, which are computed using four different time steps $\delta t = 1, 0.1, 0.01$, and 0.001 , respectively. The investigated simulation has been performed until $T = 100$. Note that the total energy has been normalized by the initial energy. All the energy evolution curves follow a monotonic decay trend, which indicate that our proposed method is stable.

4.3. Dendrite crystal growth with fourfold anisotropy

In this example, we study how the position of the initial nucleus can affect the shape of the dendritic crystal. The initial condition is given as

$$\begin{aligned} \phi(x, y, t = 0) &= \tanh\left(\frac{0.02 - \sqrt{(x - \pi)^2 + (y - \pi)^2}}{0.072}\right), \\ \theta(x, y, t) &= 0, \\ T(x, y, t = 0) &= \begin{cases} -0.55, & \text{if } \phi > 0, \\ 0, & \text{otherwise.} \end{cases} \end{aligned} \quad (26)$$

In Fig. 3(a), we display the temporal evolutions of the phase variable at different times with $K = 0.8$ and $\delta t = 0.01$. Because of the anisotropic effects, we observe that the growth of the crystalline phase becomes an anisotropic shape without

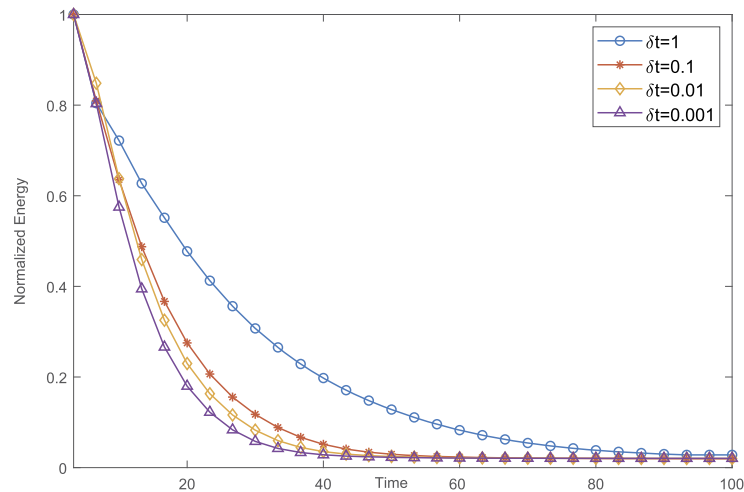


Fig. 2. Time evolutions of total free energy with the initial conditions (24) and various time steps computed by our method. Note that the total energy has been normalized by the initial energy.

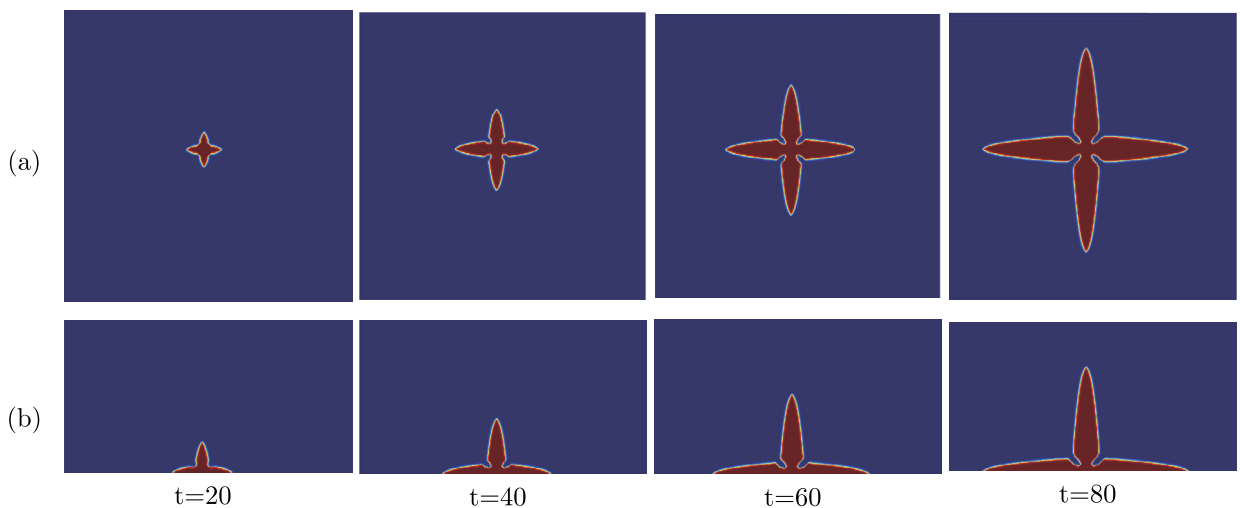


Fig. 3. The temporal evolution of dendritic crystal growth process with $K = 0.8$ and the time step $\delta t = 0.01$. From top to bottom, (a) and (b) are the location initial nucleus that is centre and bottom, respectively. From left to right, snapshots of the numerical approximation are taken at time = 20, 40, 60, 80, respectively.

orientations. In Fig. 4(a), we display the distribution of the temperature field T that agrees well with the phase field variable ϕ . Next, we conduct a computational experiment with the zero Neumann boundary condition. In Fig. 3(b), we set the y -direction boundary condition to be zero Neumann and keep the x -direction boundary condition to be periodic. The initial nucleus is located at the bottom. In Fig. 3(b), the crystal nucleus grows to the half of the dendrite pattern with four branches. Fig. 4(b) shows the temporal evolutions of the temperature field. Fig. 3(a) and (b) demonstrate that our proposed method can assure the consistency of partial evolution and whole evolution of crystal.

4.4. Evolution of multi-crystal growth

Let us consider multiple dendritic growth. Fig. 5(a) shows impingement and coarsening of multi-crystal. It can be observed that the evolution of the central crystal is obviously influenced by the four surrounding crystals, and the influence is mutual. The contact parts of the four surrounding crystals and the central crystal have obvious abnormal evolution. Those branching in the crystal where not region of impingement evolved normally. Eventually, the tips of five growing crystal regions change directions once they are to collide to form a liquid boundary layer. Fig. 5(b) shows the distribution of the temperature field T , which agrees well with the phase field variable ϕ due to the latent heat coupling terms. We can see that our method can capture the interface of multi-crystal collision well.

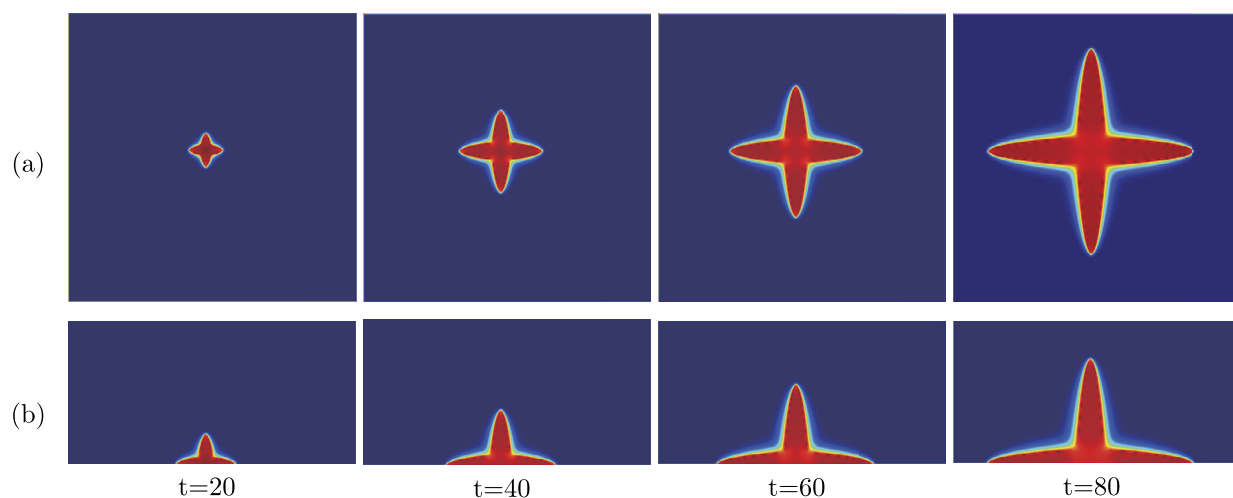


Fig. 4. (a) and (b) are the profiles of temperature T of Fig. 3(a) and (b), respectively.

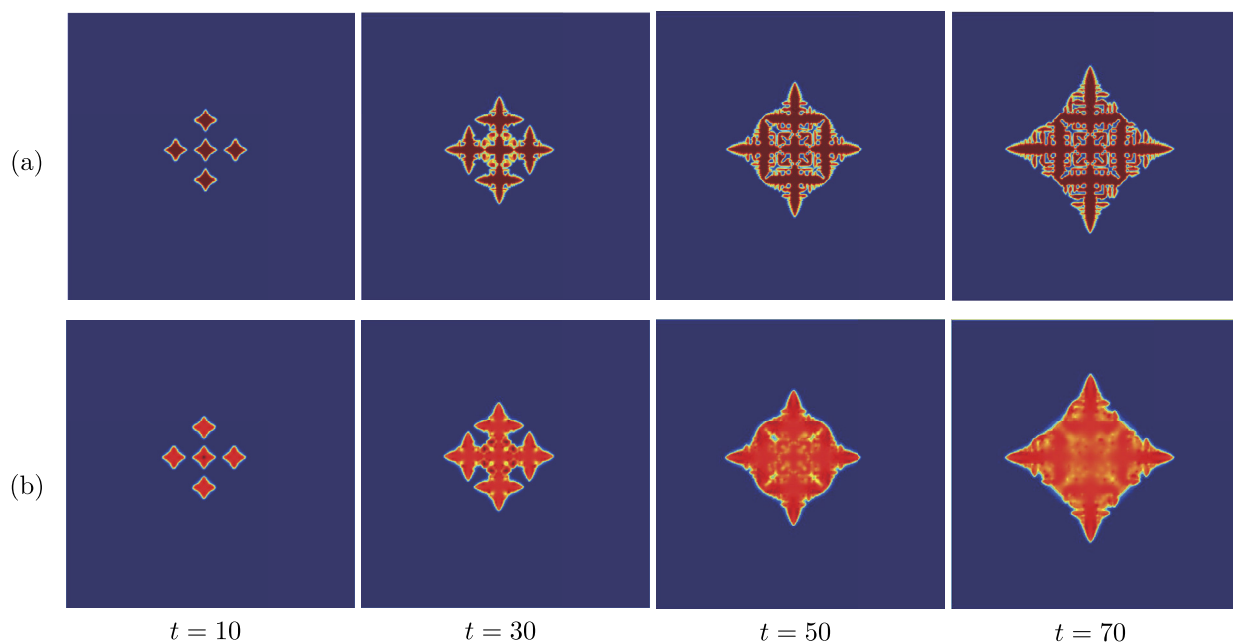


Fig. 5. The temporal evolution of dendritic crystal growth process. (a) and (b) are the profiles of the phase-field variable ϕ and temperature T , respectively.

4.5. Dendrite crystal growth with the orientational field

With the influence of the orientational field, the branching situation is different at the same time. Fig. 6(a) shows that the orientation-field enables control of crystal shapes. We can see that the orientational selection of the crystal tip is not straight but curve with periodical pattern. Fig. 7(a)–(b) show the distribution of the temperature field T , which agrees well with the phase field variable ϕ due to the latent heat coupling terms.

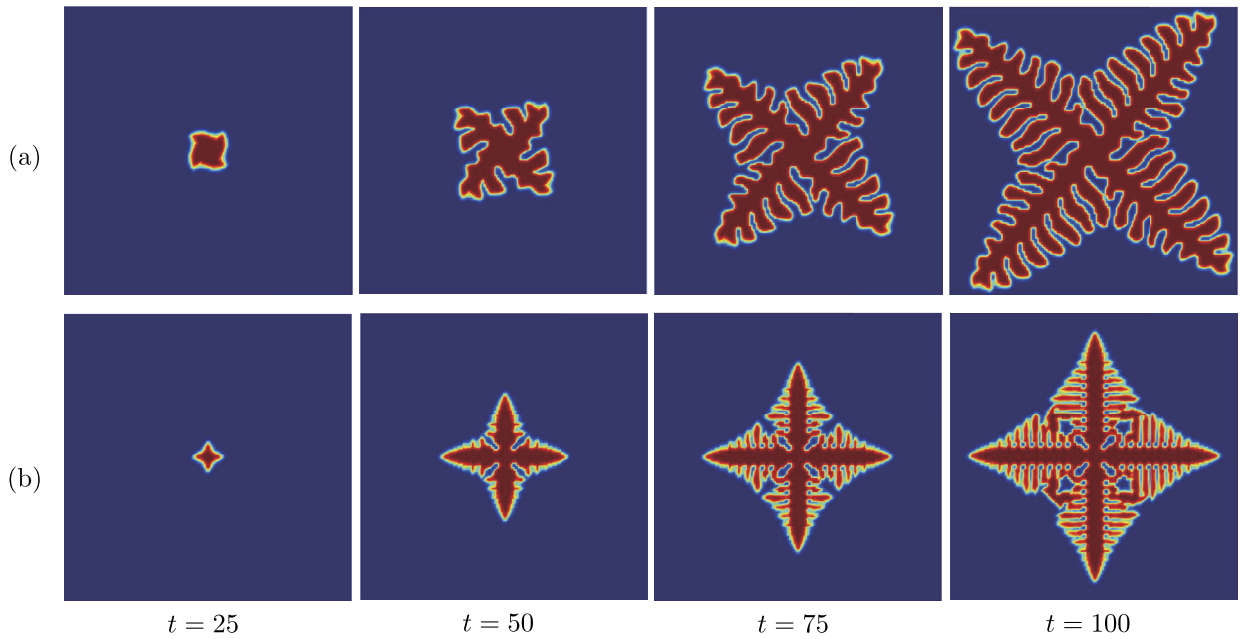


Fig. 6. The temporal evolution of dendritic crystal growth process. (a) is the profiles of the phase-field variable ϕ after coupling the orientation field. (b) is the profiles of the phase-field variable ϕ .

$$\begin{aligned}
 \phi(x, y, t = 0) &= \tanh\left(\frac{0.02 - \sqrt{(x - \pi)^2 + (y - \pi)^2}}{0.072}\right), \\
 \theta(x, y, t) &= \begin{cases} 0, & \text{if } \frac{0.05 - \sqrt{(x - \pi)^2 + (y - \pi)^2}}{0.072} > 0.02, \\ \theta_i \pi \frac{0.05 - \sqrt{(x - \pi)^2 + (y - \pi)^2}}{0.072} / \max\left(\frac{0.05 - \sqrt{(x - \pi)^2 + (y - \pi)^2}}{0.072}\right), & \text{otherwise,} \end{cases} \\
 T(x, y, t = 0) &= \begin{cases} -0.55, & \text{if } \phi > 0, \\ 0, & \text{otherwise.} \end{cases}
 \end{aligned} \tag{27}$$

4.6. Six-folds dendrite crystal growth with the orientational field

In this section, we performed the simulation with six-folds dendrite crystal growth under the influence of orientation field. We set the time step $\delta t = 0.01$ and the non-default parameter $\varepsilon_\phi = 1.5e - 2$, $s = 1.5$ and $K = 0.8$. The initial conditions are chosen as

$$\begin{aligned}
 \phi(x, y, t = 0) &= \tanh\left(\frac{0.02 - \sqrt{(x - \pi)^2 + (y - \pi)^2}}{0.072}\right), \\
 \theta(x, y, t) &= \theta_0 \left(\frac{\sin(\sqrt{(x - \pi)^2 + (y - \pi)^2})}{\sqrt{(x - \pi)^2 + (y - \pi)^2}} - 1 \right), \\
 T(x, y, t = 0) &= \begin{cases} -0.55, & \text{if } \phi > 0, \\ 0, & \text{otherwise.} \end{cases}
 \end{aligned} \tag{28}$$

Fig. 8 shows the temporal evolution of the dendritic crystal growth process with the rotational six-folds crystallization. The specific times are chosen as $t = 25$, $t = 50$, $t = 75$, and $t = 100$, respectively. The top row of Fig. 8 shows the evolution of the phase-field variable ϕ and the bottom row shows the evolution of temperature field. We can observe that with the computation times t increases, the formed crystal tips, and branches evolve along a curve. Furthermore, we applied the parameter analysis for the investigation of orientation θ . We applied this comparison test with the same initial condition for Fig. 8. Fig. 9 show the six-fold dendrites evolution. As shown in Fig. 9, from left to right, the initial orientation parameter θ_0 is chosen as 2, 4, 6 and 8, respectively. We can observe that with the parameter θ_0 increases, crystals grow into curved states while forming a pinwheel shape. Furthermore, it can be clearly seen that the development of secondary dendrite crystal demonstrates a strong coupling relationship with the orientation field.

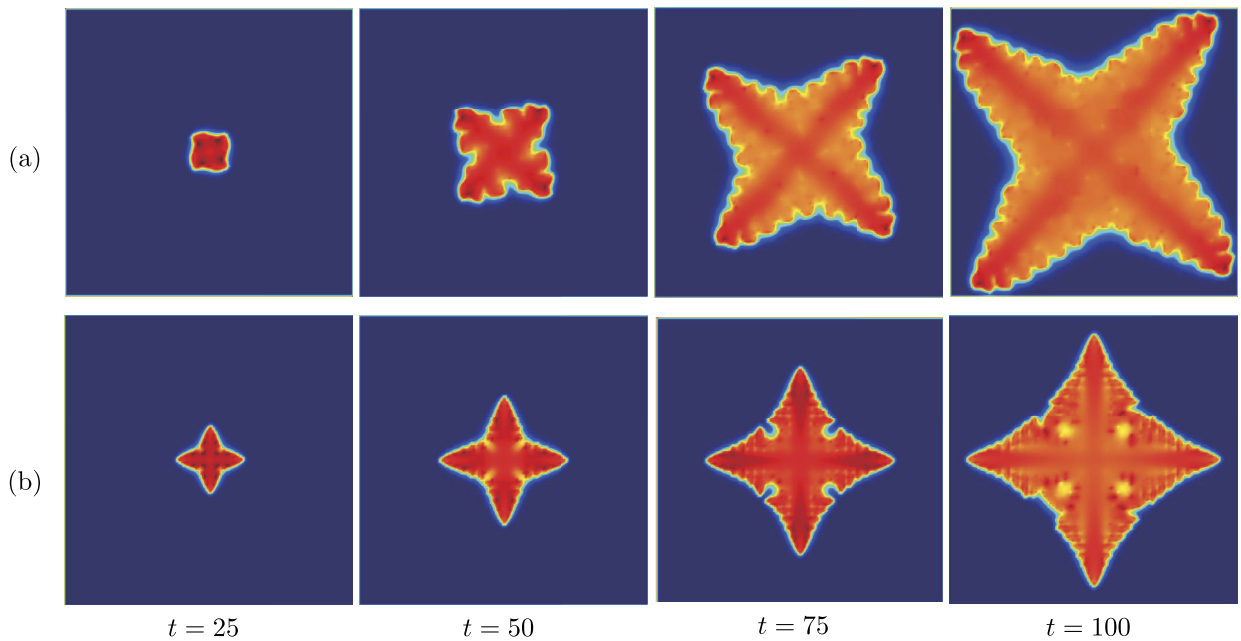


Fig. 7. The temporal evolution of crystal growth with $K = 0.7$ and the time step $\delta t = 0.01$. (a) is the profiles of the phase-field variable T after coupling the orientation field, (b) is the profiles of the phase-field variable T .

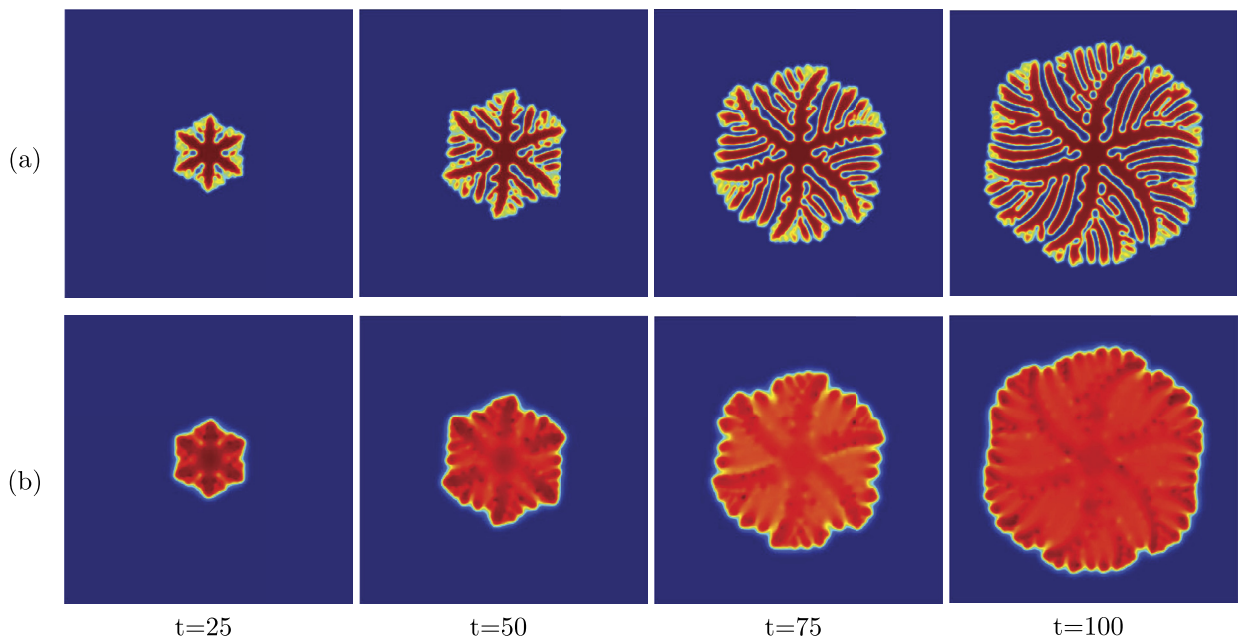


Fig. 8. The temporal evolution of dendritic crystal growth process, with condition(28), $K = 0.8$ and the time step $\delta t = 0.01$. (a) is the profiles of the phase-field variable ϕ after coupling the orientation field, (b) is the profiles of the phase-field variable T .

4.7. Dendrite crystal coupled with multi-orientational field

We consider a situation where multiple dendrites grow simultaneously with nucleus from different locations and their respective orientational field. We choose time step $\delta t = 0.01$, parameters $s = 0$ and $K = 0.7$. As shown in Fig. 10 and 11, from left to right and from the top down, the label of crystal is set as 1, 2, 3, 4. Fig. 10(a) shows the evolution of four crystals under the same initial condition (Eq. (27)) with $\theta_i = 5$, ($i = 1, 2, 3, 4$). Fig. 11(a) shows the evolution of four crystals under the same initial condition (Eq. (27)) with $\theta_i = 5$, ($i = 1, 2, 3, 4$). With the influence of the same orientation parameter, Fig. 10(a) shows the evolution and coarsening of the four crystals. We can see that the four crystals impingement in the

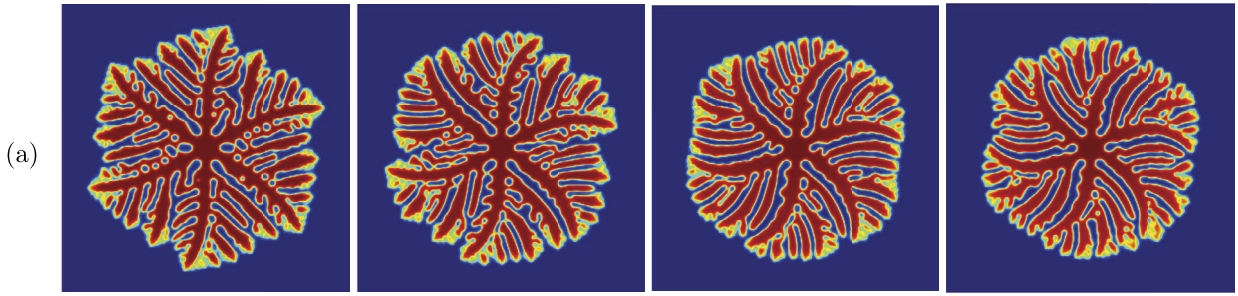


Fig. 9. (a) is the profiles of the phase-field variable ϕ after coupling the orientation field. From left to right, the parameter θ_0 is 2, 4, 5, 8, respectively.

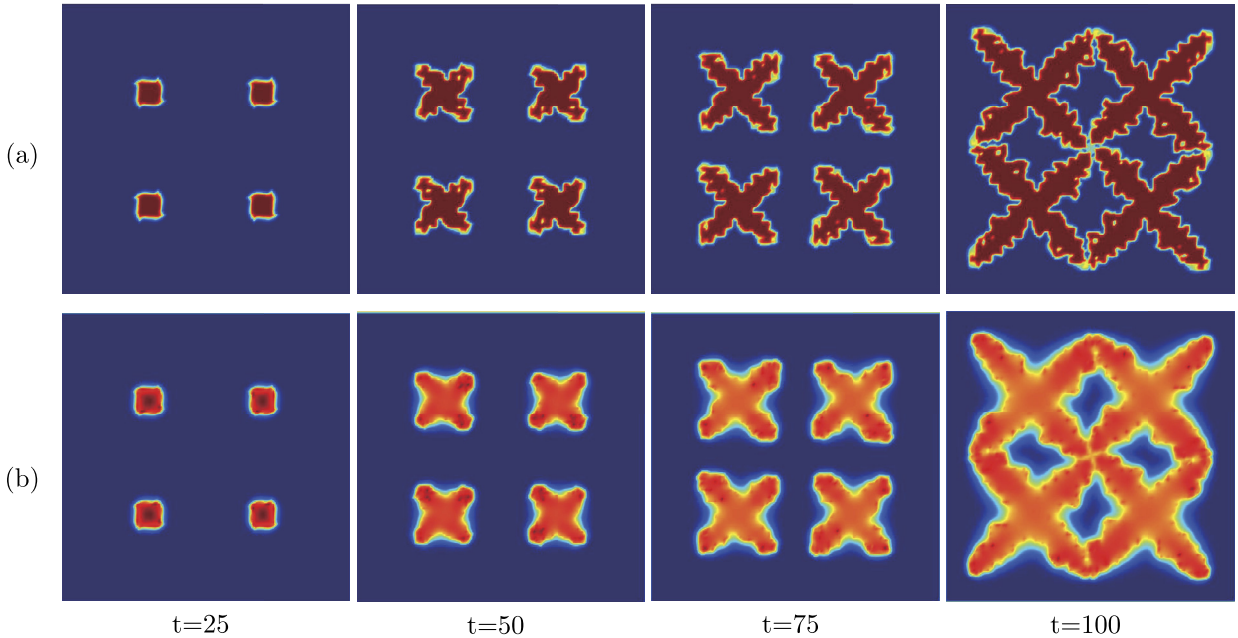


Fig. 10. The temporal evolution of dendritic crystal growth process, with $K = 0.7$ and the time step $\delta t = 0.01$. (a) is the profiles of the phase-field variable ϕ after coupling the orientation field. (b) is the profiles of the phase-field variable T .

central of domain. With the influence of the difference orientational field, Fig. 11(a) shows the evolution and coarsening of the four crystals. We can see that only the top two of four crystals impingement in the top of computational domain. It can be seen from Fig. 10(a) and Fig. 11(a) that the orientational field has an impact on the location and angle of collision of multi-crystal. We can see that our method can capture the interface of multi-crystal collision well.

4.8. 3D dendrite crystal growth with fourfold anisotropy property

In this section, we demonstrate the 3D dendrite crystal growth with the fix orientation considering the fourfold anisotropic property. The computational domain is chosen as $\Omega = [0, 2\pi] \times [0, 2\pi] \times [0, 2\pi]$ with a $512 \times 512 \times 512$ mesh grid. The non-default parameters are chosen as $K = 1$. We choose the time step as $\delta t = 0.01$ and the initial condition as follows:

$$\begin{aligned} \phi(x, y, t = 0) &= \tanh\left(\frac{0.02 - \sqrt{(x - \pi)^2 + (y - \pi)^2 + (z - \pi)^2}}{0.072}\right) \\ T(x, y, t = 0) &= \begin{cases} -0.55, & \text{if } \phi > 0 \\ 0, & \text{otherwise.} \end{cases} \end{aligned} \quad (29)$$

Fig. 12 shows the temporal evolution of dendritic crystal growth process in 3D space. From left to right, they are the results at times $t = 0, 12, 48, 144, 324$, and 444 , respectively. It can be seen that the proposed algorithm can work well for simulating the crystal growth in the three-dimensional space.

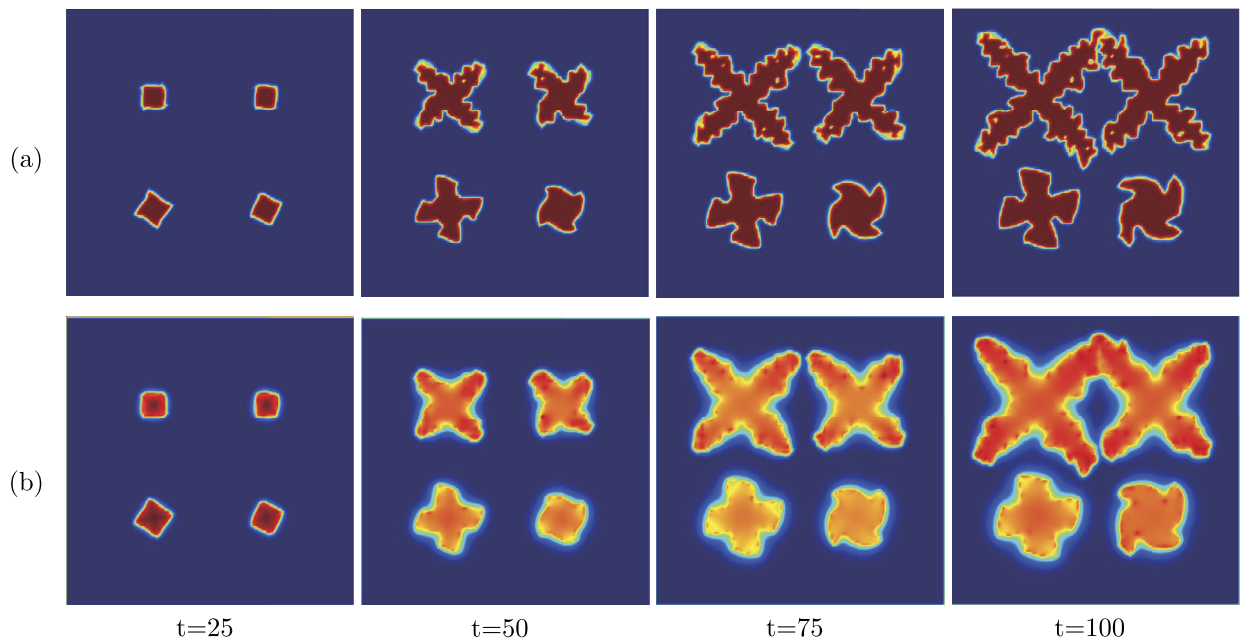


Fig. 11. The temporal evolution of dendritic crystal growth process, with $K = 0.7$ and the time step $\delta t = 0.01$. (a) is the profiles of the phase-field variable ϕ after coupling the orientation field, (b) is the profiles of the phase-field variable T .

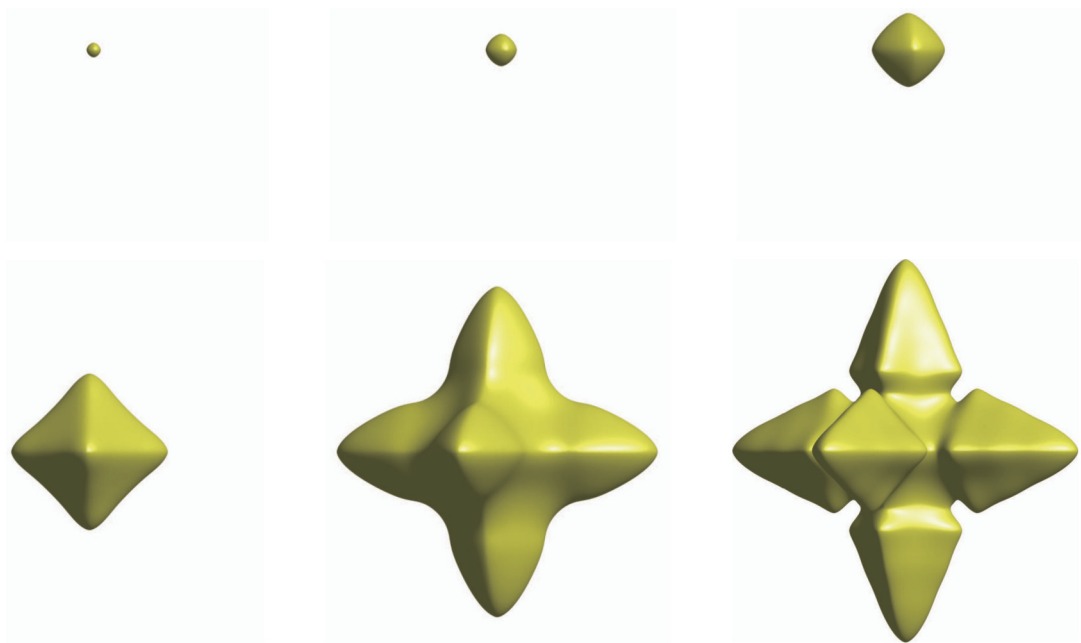


Fig. 12. The temporal evolution of dendritic crystal growth process in 3D space. The specific times are chosen as $t = 0, 12, 48, 144, 324$, and 444 , respectively.

5. Conclusion

In this study, we presented an efficient, semi-discrete in time, second-order, linear scheme for solving the anisotropic dendritic phase field equation with the orientation-field using the developed IEQ approach. Some auxiliary variables were introduced to transform the governing system into an equivalent equation, which allowed the nonlinear potential to be treated efficiently and semi-explicitly. The proposed schemes was unconditionally energy stable without adding stabilizers, which allowed us to use large time steps. Specifically, the discrete schemes were linear and decoupled, which were easy to implement. Numerical results demonstrated that our numerical scheme could simulate the evolution of the crystal coupling

the orientation field, for instances, impingement and coarsening, which confirmed the efficiency and stability of the developed schemes. Three-dimensional crystal growth should be coupled by two mutually orthogonal orientation fields, which is extremely complex. As the future research, we will consider the 3D crystal growth simulations with time-depend multiple orientation. Furthermore, following Yang et al. [41]'s framework, we will try to investigate the stability of phase variable in H_1 space.

Acknowledgements

Y.B. Li is supported by the Fundamental Research Funds for the Central Universities (No. XTR042019005). The corresponding author (J.S. Kim) was supported by Korea University Grant. The authors are grateful to the reviewers whose valuable suggestions and comments significantly improved the quality of this paper.

References

- [1] L.-Q. Chen, Phase-field models for microstructure evolution, *Annu. Rev. Mater. Res.* 32 (1) (2002) 113–140.
- [2] K.R. Elder, N. Provatas, J. Berry, P. Stefanovic, M. Grant, Phase-field crystal modeling and classical density functional theory of freezing, *Phys. Rev. B* 75 (2007) 064107.
- [3] K. Fujiwara, W. Pan, N. Usami, K. Sawada, M. Tokairin, Y. Nose, A. Nomura, T. Shishido, K. Nakajima, Growth of structure-controlled polycrystalline silicon ingots for solar cells by casting, *Acta Mater.* 54 (12) (2006) 3191–3197.
- [4] M. Gäumann, C. Bezencon, P. Canalis, W. Kurz, Single-crystal laser deposition of superalloys: processing–microstructure maps, *Acta Mater.* 49 (6) (2001) 1051–1062.
- [5] Y. Gong, J. Zhao, Energy-stable Runge–Kutta schemes for gradient flow models using the energy quadratization approach, *Appl. Math. Lett.* 94 (2019) 224–231.
- [6] Y. Gong, J. Zhao, Q. Wang, Arbitrarily high-order linear energy stable schemes for gradient flow models, *J. Comput. Phys.* 419 (2020) 109610.
- [7] L. Gránásy, L. Rátkai, A. Szállás, B. Korbuly, G.I. Tóth, L. Környei, T. Pusztai, Phase-field modeling of polycrystalline solidification: from needle crystals to spherulites—a review, *Metall. Mater. Trans., A* 45 (2014) 1694–1719.
- [8] L. Grech, B. Mallia, J. Camilleri, Investigation of the physical properties of tricalcium silicate cement-based root-end filling materials, *Dent. Mater.* 29 (2013) e20–e28.
- [9] Z. Hu, S.M. Wise, C. Wang, J.S. Lowengrub, P. Nikolas, G. Nigel, D. Jonathan, Efficient computation of dendritic microstructures using adaptive mesh refinement, *Phys. Rev. Lett.* 80 (1998) 3308.
- [10] Z. Hu, S.M. Wise, C. Wang, J.S. Lowengrub, Stable and efficient finite-difference nonlinear-multigrid schemes for the phase field crystal equation, *J. Comput. Phys.* 228 (2009) 5323–5339.
- [11] A. Karma, W.-J. Rappel, Phase-field model of dendritic sidebranching with thermal noise, *Phys. Rev. E* 60 (1999) 3614.
- [12] R. Kobayashi, J.A. Warren, W.C. Carter, A continuum model of grain boundaries, *Physica D* 140 (2000) 141–150.
- [13] B. Korbuly, T. Pusztai, G.I. Tóth, H. Henry, M. Plapp, L. Gránásy, Orientation-field models for polycrystalline solidification: grain coarsening and complex growth forms, *J. Cryst. Growth* 457 (2017) 32–37.
- [14] W. Kurz, D. Fisher, *Fundamentals of Solidification*, Trans. Tech. Pub., Aedermannsdorf, 1998, pp. 234–235.
- [15] J. Li, J. Wang, G. Yang, Phase-field simulation of microstructure development involving nucleation and crystallographic orientations in alloy solidification, *J. Cryst. Growth* 309 (2007) 65–69.
- [16] J. Li, J. Zhao, Q. Wang, Energy and entropy preserving numerical approximations of thermodynamically consist crystal growth models, *J. Comput. Phys.* 382 (2019) 202–220.
- [17] Y. Li, J. Kim, Phase-field simulations of crystal growth with adaptive mesh refinement, *Int. J. Heat Mass Transf.* 55 (2012) 7926–7932.
- [18] Y. Li, H.G. Lee, J. Kim, A fast, robust, and accurate operator splitting method for phase-field simulations of crystal growth, *J. Cryst. Growth* 321 (1) (2011) 176–182.
- [19] Y. Li, Q. Xia, S. Yoon, C. Lee, B. Lu, J. Kim, Simple and efficient volume merging method for triply periodic minimal structures, *Comput. Phys. Commun.* 264 (2021) 107956.
- [20] Y. Li, K. Wang, Q. Yu, Q. Xia, J. Kim, Unconditionally energy stable schemes for fluid-based topology optimization, *Commun. Nonlinear Sci.* 111 (2022) 106433.
- [21] Y. Li, Q. Xia, C. Lee, S. Kim, J. Kim, A robust and efficient fingerprint image restoration method based on a phase-field model, *Pattern Recognit.* 123 (2022) 108405.
- [22] J. Shen, X. Yang, Numerical approximations of Allen–Cahn and Cahn–Hilliard equations, *Discrete Cont. Dyn.-A* 28 (2010) 1669–1691.
- [23] J. Shen, J. Xu, J. Yang, The scalar auxiliary variable (sav) approach for gradient flows, *J. Comput. Phys.* 353 (2018) 407–416.
- [24] I. Singer-Loginova, H. Singer, The phase field technique for modeling multiphase materials, *Rep. Prog. Phys.* 71 (2008) 106501.
- [25] P. Stefanovic, M. Haataja, N. Provatas, Phase field crystal study of deformation and plasticity in nanocrystalline materials, *Phys. Rev. E* 80 (2009) 046107.
- [26] S. Sun, J. Li, J. Zhao, Q. Wang, Structure-preserving numerical approximations to non-isothermal hydrodynamic model of binary fluid flows, *J. Sci. Comput.* 83 (2020) 1–43.
- [27] I. Tamas, Full-discretization and semi-discretization for milling stability prediction: some comments, *Int. J. Mach. Tool. Manu.* 50 (2010) 658–662.
- [28] S. Tang, Z. Wang, Y. Guo, J. Wang, Y. Yu, Y. Zhou, Orientation selection process during the early stage of cubic dendrite growth: a phase-field crystal study, *Acta Mater.* 60 (2012) 5501–5507.
- [29] S. Tang, Y.-M. Yu, J. Wang, J. Li, Z. Wang, Y. Guo, Y. Zhou, Phase-field-crystal simulation of nonequilibrium crystal growth, *Phys. Rev. E* 89 (2014) 012405.
- [30] M. Totir, N. Echols, M. Nanao, C.L. Gee, A. Moskaleva, S. Gradia, A.T. Lavarone, J.M. Berger, A.P. May, C. Zubieta, T. Alber, Macro-to-micro structural proteomics: native source proteins for high-throughput crystallization, *PLoS ONE* 7 (2012) e32498.
- [31] S.-L. Wang, R. Sekerka, A. Wheeler, B. Murray, S. Coriell, R. Braun, G. McFadden, Thermodynamically-consistent phase-field models for solidification, *Physica D* 69 (1993) 189–200.
- [32] J.A. Warren, W.J. Boettinger, Prediction of dendritic growth and microsegregation patterns in a binary alloy using the phase-field method, *Acta Metall. Mater.* 43 (1995) 689–703.
- [33] J.A. Warren, R. Kobayashi, A.E. Lobkovsky, W.C. Carter, Extending phase field models of solidification to polycrystalline materials, *Acta Mater.* 51 (2003) 6035–6058.
- [34] J.D. Weeks, G.H. Gilmer, Dynamics of crystal growth, *Adv. Chem. Phys.* 40 (1979) 157–228.

- [35] D. Winn, M.F. Doherty, Modeling crystal shapes of organic materials grown from solution, *AIChE J.* 46 (7) (2000) 1348–1367.
- [36] Q. Xia, Q. Yu, Y. Li, A second-order accurate, unconditionally energy stable numerical scheme for binary fluid flows on arbitrarily curved surfaces, *Comput. Methods Appl. Math.* 384 (2021) 113987.
- [37] Q. Xia, J. Kim, Y. Li, Modeling and simulation of multi-component immiscible flows based on a modified Cahn-Hilliard equation, *Eur. J. Mech. B, Fluids* 95 (2022) 194–204.
- [38] J. Yang, Z. Tan, J. Kim, High-order time-accurate, efficient, and structure-preserving numerical methods for the conservative Swift-Hohenberg model, *Comput. Math. Appl.* 102 (2021) 160–174.
- [39] J. Yang, J. Chen, Z. Tan, Highly efficient variant of sav approach for two-phase incompressible conservative Allen-Cahn fluids, *Eng. Comput.* (2022) 1–19.
- [40] J. Yang, Z. Tan, J. Kim, Linear and fully decoupled scheme for a hydrodynamics coupled phase-field surfactant system based on a multiple auxiliary variables approach, *J. Comput. Phys.* 452 (2022) 110909.
- [41] X. Yang, Efficient linear, stabilized, second-order time marching schemes for an anisotropic phase field dendritic crystal growth model, *Comput. Methods Appl. Math.* 347 (2019) 316–339.
- [42] X. Yang, Fully-discrete spectral-Galerkin scheme with decoupled structure and second-order time accuracy for the anisotropic phase-field dendritic crystal growth model, *Int. J. Heat Mass Transf.* 180 (2021) 121750.
- [43] X. Yang, On a novel full decoupling, linear, second-order accurate, and unconditionally energy stable numerical scheme for the anisotropic phase-field dendritic crystal growth model, *Int. J. Numer. Methods Eng.* 122 (2021) 4129–4153.
- [44] X. Yang, J. Zhao, Q. Wang, Numerical approximations for the molecular beam epitaxial growth model based on the invariant energy quadratization method, *J. Comput. Phys.* 333 (2017) 104–127.
- [45] F. Yu, Y. Wei, Y. Ji, L.-Q. Chen, Phase field modeling of solidification microstructure evolution during welding, *J. Mater. Process. Technol.* 255 (2018) 285–293.
- [46] Q. Yu, Q. Xia, Y. Li, A phase field-based systematic multiscale topology optimization method for porous structures design, *J. Comput. Phys.* 466 (2022) 111383.
- [47] Y. Yu, L. Wang, J. Zhou, H. Li, Y. Li, W. Yan, F. Lin, Impact of fluid flow on the dendrite growth and the formation of new grains in additive manufacturing, *Addit. Manuf.* 55 (2022) 102832.
- [48] J. Zhang, X. Yang, A fully decoupled, linear and unconditionally energy stable numerical scheme for a melt-convective phase-field dendritic solidification model, *Comput. Methods Appl. Math.* 363 (2020) 112779.
- [49] J. Zhang, C. Chen, X. Yang, A novel decoupled and stable scheme for an anisotropic phase-field dendritic crystal growth model, *Appl. Math. Lett.* 95 (2019) 122–129.
- [50] J. Zhao, A revisit of the energy quadratization method with a relaxation technique, *Appl. Math. Lett.* 120 (2021) 107331.
- [51] J. Zhao, Q. Wang, X. Yang, Numerical approximations for a phase field dendritic crystal growth model based on the invariant energy quadratization approach, *Int. J. Numer. Methods Eng.* 110 (2017) 279–300.